J Mater Sci (2017) 52:13012–13022

Ceramics

Band gap reduction and redshift of lattice vibrational spectra in Nb and Fe co-doped PLZT

Shibnath Samanta[1], Miryala Muralidhar[3], V. Sankaranarayanan[1], K. Sethupathi[1,*], M. S. Ramachandra Rao[2], and Masato Murakami[3]

[1] *Department of Physics, Indian Institute of Technology Madras (IITM), Chennai 600036, India*
[2] *Nano-Functional Materials Technology Centre, Indian Institute of Technology Madras (IITM), Chennai 600036, India*
[3] *Graduate School of Science and Engineering, Superconducting Materials Laboratory, Shibaura Institute of Technology, 3-7-5 Toyosu, Koto-ku, Tokyo 135-8548, Japan*

Received: 18 May 2017
Accepted: 24 July 2017

ABSTRACT

Nb and Fe co-doped PLZT ($Pb_{0.97}La_{0.02}(Zr_{0.52}Ti_{0.48})_{1-2x}(Nb_{0.5}Fe_{0.5})_{2x}O_3$ for $x = 0.00$, 0.02, 0.04, 0.06 and 0.08) samples have been prepared using sol–gel method. X-ray diffraction (XRD) and Raman spectroscopy studies confirmed that the samples are single phase even for the highest tested doping of 8 mol% of Nb and Fe. Incorporation of Nb and Fe atoms into PLZT lattice has been confirmed by XRD study where a systematic peak shift has been observed with increasing dopant concentration. The lattice parameters are found to decrease gradually with increase in Nb and Fe contents. From Raman spectroscopic investigation, redshift of several modes has been observed. Rietveld refinement has been performed to correlate XRD results with the fitting of Raman spectra. A total of 14 distinguished modes have been identified by de-convolution of Raman spectra, and they are in good agreement with the theoretically calculated modes for $PbTiO_3$ and also with those reported on PZT and PLZT previously. The Burstein–Moss shift of absorption edge has been observed by diffuse reflectance spectroscopy experiment, and the analysis shows change in band gap from 3.21 eV (for $x = 0.00$) to 2.59 eV (for $x = 0.08$). The underlying mechanisms and the observed electronic behavior have been confirmed and analyzed by photoluminescence study which revealed several transitions and supported the effect of Nb and Fe co-doping as observed from XRD and Raman spectroscopy.

Introduction

At present, lead zirconate titanate [$Pb(Zr_{1-x}Ti_x)O_3$, known as PZT] and its modified compositions are in high demand in industries due to their versatile device applications like FeRAM, DRAM and display devices. In addition, these materials are also used in electro-optical modulators, pyroelectric and gas sensors, transducers, hydrophones, other electronic and optoelectronic applications with high efficiency and

---

Address correspondence to E-mail: ksethu@iitm.ac.in

DOI 10.1007/s10853-017-1425-7

tunability. PZT is an ABO_3-type perovskite oxide and a solid solution of $PbZrO_3$ and $PbTiO_3$. Among the compositions in the range from $x = 0$ to 1 for $Pb(Zr_{1-x}Ti_x)O_3$, the composition with $x = 0.48$ exhibits enhanced ferroelectric, piezoelectric and dielectric properties. At this composition, ($PbZr_{0.52}Ti_{0.48}O_3$ [PZT(52/48)]) exhibits the morphotropic phase boundary (MPB) between Zr-rich rhombohedral and Ti-rich tetragonal phases [1–5]. As researchers continue to explore and enhance the properties of PZT by the modification of A-site, as well as B-site with suitable elements, many new properties and application possibilities are evolving.

Multiferroics offer the possibilities of fast low power electrical writing with nondestructive magnetic writing operation in a combination of high-quality FeRAM and MRAMs [6]. Hence, a trend to get multiferroics at room temperature has become more interesting and popular. Room temperature multiferroic nature has been found to be limited to fewer materials like $BiFeO_3$, $CdSr_2S_4$, $LuFe_2O_4$, $RMnO_3$, RMn_2O_5 and boracites. There have been several attempts to convert ferroelectrics into multiferroics either by introducing magnetic dopants [7, 8] or by making ferroelectric–ferromagnetic composite systems [9–16]. Xu et al. [7] reported that $BaTiO_3$ (one of the most popular ferroelectric materials) exhibits ferroelectricity as well as ferromagnetism at room temperature upon Fe doping. Around this time, Kleebe et al. [8] successfully demonstrated the preparation and characterization of 3 mol% Fe-doped PZT(60/40) which is above the solubility limit (approximately 1 mol%). Recently, room temperature multiferroic properties of Nb- and Ta-doped PZT near MPB composition are reported by Schiemer et al. [17]. In this case, both Nb and Ta are co-doped, each up to 2 mol%.

The present work deals with the preparation and characterization of Fe and Nb co-doped (up to 8 mol% each) PLZT. Rietveld refinement was performed to confirm the phase purity and understand the impact of Nb and Fe co-doping on structural changes. In the first decade of the twenty first century, intense use of Raman spectroscopy for characterization of PZT-based materials has been seen [18–29]. With the help of those earlier reports and multiple peaks fitting of Raman spectral data, the successful incorporation of Nb and Fe in PLZT lattice is confirmed. A detailed lattice vibrational analysis clearly shows that it is possible to incorporate up to 6 mol% of Fe and Nb together in PLZT. However, doping of 8 mol% of Fe and Nb exhibits marginal effect with respect to the changes observed for the sample with 6 mol% doping in Raman spectroscopy. Band gap tuning is a very important technology, and in particular, tailoring band gap of large band gap semiconductors renders them useful for several applications. In this study, Nb and Fe co-doping is found to be very effective in the reduction in band gap of PLZT.

Experimental details

Samples of $Pb_{0.97}La_{0.02}(Zr_{0.52}Ti_{0.48})_{1-2x}(Nb_{0.5}Fe_{0.5})_{2x}O_3$ for $x = 0.00$, 0.02, 0.04, 0.06 and 0.08 (abbreviated as NF0, NF2, NF4, NF6 and NF8, respectively) are prepared by sol–gel synthesis following the steps shown in the flowchart (Fig. 1).

All chemicals used for the preparation of PLZT (NF0, NF2, NF4, NF6 and NF8) are procured from Sigma-Aldrich. Lead(II) acetate trihydrate (99.999%) and Lanthanum(III) acetate hydrate (99.9%) are added to glacial acetic acid and stirred to get a homogeneous solution. In another beaker, Niobium(V) ethoxide (99.95%) is added to glacial acetic acid and stirred for an hour. Then Zirconium(IV) propoxide solution (70 wt% in 1-propanol), Titanium(IV) isopropoxide (97%) and Ferric nitrate are added to the niobium ethoxide–acetic acid solution one after the other with continuous stirring. Ferric(III) nitrate nonahydrate (99.95%) is turned into aqueous solution before adding. After stirring at room temperature for about 30 min, these two solutions are mixed. The mixture looks milky white in color at room temperature. Then, the temperature is increased slowly to 90 °C with continuous stirring, and after a few minutes, the solution gradually becomes colorless. The solution is kept at this temperature until it becomes white powder via thick gel formation. It takes almost 96 h for the thick gel to become dry powder. The white powder is ground and then calcined at 700 °C for 1 h. This has led to an orange color PLZT powder.

X-ray diffraction(XRD) studies are carried out using Rigaku SmartLab diffractometer with Cu K_α radiation ($\lambda = 1.5406$ Å), and Raman spectroscopic studies are carried out in LabRAM HR spectrometer (Horiba Jobin–Yvon, France) with the help of LabSpec 6 software. The DRS and PL experiments are

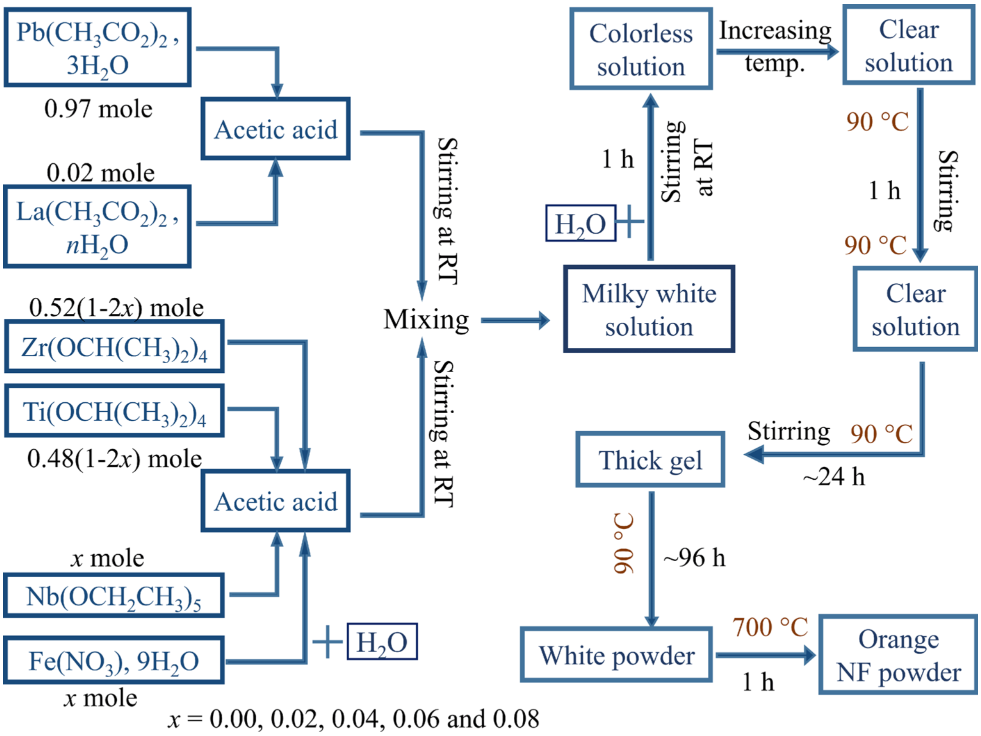

Figure 1 Flowchart of sol–gel synthesis of Nb and Fe co-doped PLZT (NF0, NF2, NF4, NF6 and NF8).

performed using Bentham TMc300 monochromator and Horiba Fluorolog-3.

Results and discussion

Structural analysis

Phase purity of the samples is determined by XRD analysis, and the results are shown in Fig. 2. XRD patterns indicate that the samples exhibit perovskite structure without the presence of any secondary phases like pyrochlore or phases related to niobium and iron oxides. XRD results confirm the formation of tetragonal structure, as they are in good agreement with the previously reported tetragonal PZT. The patterns are indexed using well-matched JCPDS card #33-0784 and COD ID 1526174. The absence of any impurity phase confirms the successful incorporation of Nb and Fe in PLZT lattice. A systematic change with doping concentration of Nb and Fe is observable in the closer view (Fig. 2b–d) of the first three peaks. Due to doping of 8 mol% of Nb and Fe, the (100) peak shifted toward higher 2θ by about 0.13°. Similar shifts are also observed for (110) and (111) peaks. The shift in 2θ value for these two peaks is around 0.16°. The shifts for all the peaks are toward higher 2θ. The shift is prominent at lower 2θ values while at higher angles the shift is not so prominent due to the fact that the intensity is relatively low and peak width is high at higher 2θ. There are many reasons which could be responsible for this effect. Some of the possible technical sources which may cause peak shift are avoided/minimized by taking precautions which include "optics alignment" prior to the start of the experiment. Rietveld refinement has also been performed using FullProf suite to get an insight into the peak shift. The results reveal that the lattice parameters are reduced upon Nb and Fe doping. For NF0, the lattice parameters a and c are found to be 4.0644 and 4.0995 Å, respectively, which decrease to 4.0536 and 4.0808 Å, respectively, in NF8 (Fig. 3). Hence, the unit cell volume has been found to decrease from 67.72 to 67.05 Å^3 due to 8 mol% co-doping of Nb and Fe. The Nb^{5+} and Fe^{3+} have crystal ionic radii ~78 and 69 pm, respectively (effective ionic radii ~64 and 55 pm, respectively), while the corresponding values for Zr^{4+} and Ti^{4+} are 86 and 74.5 pm, respectively (effective ionic radii ~72 and 60.5 pm, respectively). This suggests that doping of smaller ions causes shrinkage of the unit cells. Hence, the shift in peaks toward higher 2θ values can be attributed to decrease in the lattice parameters.

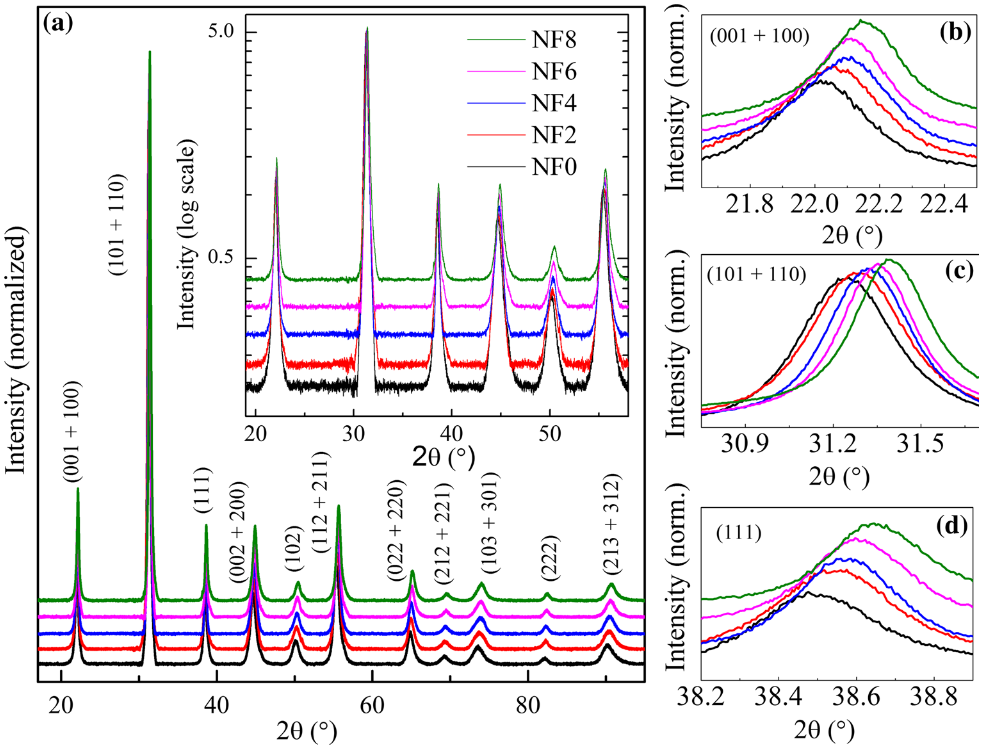

Figure 2 XRD results for Nb and Fe co-doped PLZT. **a** "*Inset*" shows the plot of the dataset with vertical log scale. **b**–**d** Show the zoomed view of the shifting of peaks with doping concentration.

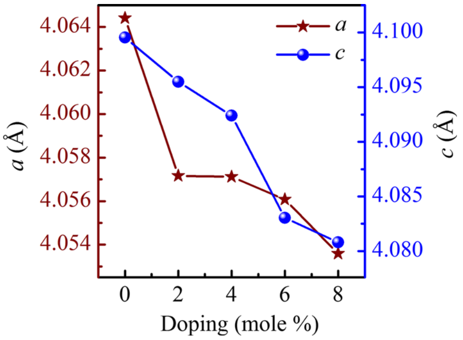

Figure 3 Change in lattice parameters due to change in the doping concentration of Nb and Fe co-doped PLZT, as calculated by Rietveld refinement using FullProf suite.

Analysis of lattice vibrations

Raman spectra recorded for NF0, NF2, NF4, NF6 and NF8 are shown in Fig. 4. The results exhibit well-distinguished phonon modes including the "soft modes." In order to detect visible changes, which occur due to gradual incorporation of Nb and Fe into PLZT lattice, the energy range from 20 to 1000 cm^{-1} is divided into several regions and plotted separately with closer view (A, D, E and F in Fig. 4). The spectra for NF0 show both the soft modes in the frequency range between 50 and 100 cm^{-1} (A in Fig. 4) having nearly equal intensity, while the peak around 76 cm^{-1} gains relatively higher intensity with increasing Nb and Fe contents. The peaks around 106 and 138 cm^{-1} (marked as B and C) are visible in the case of NF0 and, however, seem to disappear due to Nb and Fe doping and the regions become smooth. The panel D shows another two peaks that have lesser intensity and larger FWHM due to incorporation of dopants. The broad peaks around 580 and 730 cm^{-1} (panel E and F in Fig. 4) show redshift for doping up to 6 mol%, and interestingly, the shift is smaller in case of NF8.

In order to identify the phonon modes and analyze their characteristic changes, the spectra are de-convoluted to individual peaks. Ferroelectric tetragonal phase with space group C_{4v}^{1} ($P4\,mm$) has $3A_1 + 4E$ polar modes and B_1 nonpolar modes. Each polar mode has transverse optical (TO) and longitudinal optical (LO) branches. Hence, there are 15 modes labeled with suffix number 1–4 according to their position in frequency spectrum from low to high. All these modes along with another three modes (E(TO), E(TA) and A_1(TA)) mentioned by Freire and Katiyar [30] are listed in Table 1. For the pure PLZT(2/52/48), i.e., NF0, the modes are shown in Fig. 5. The identified and indexed modes are compared with earlier reports in the table. The mode observed at 57 cm^{-1} can be either E(TA) [30] or a bandpass [28].

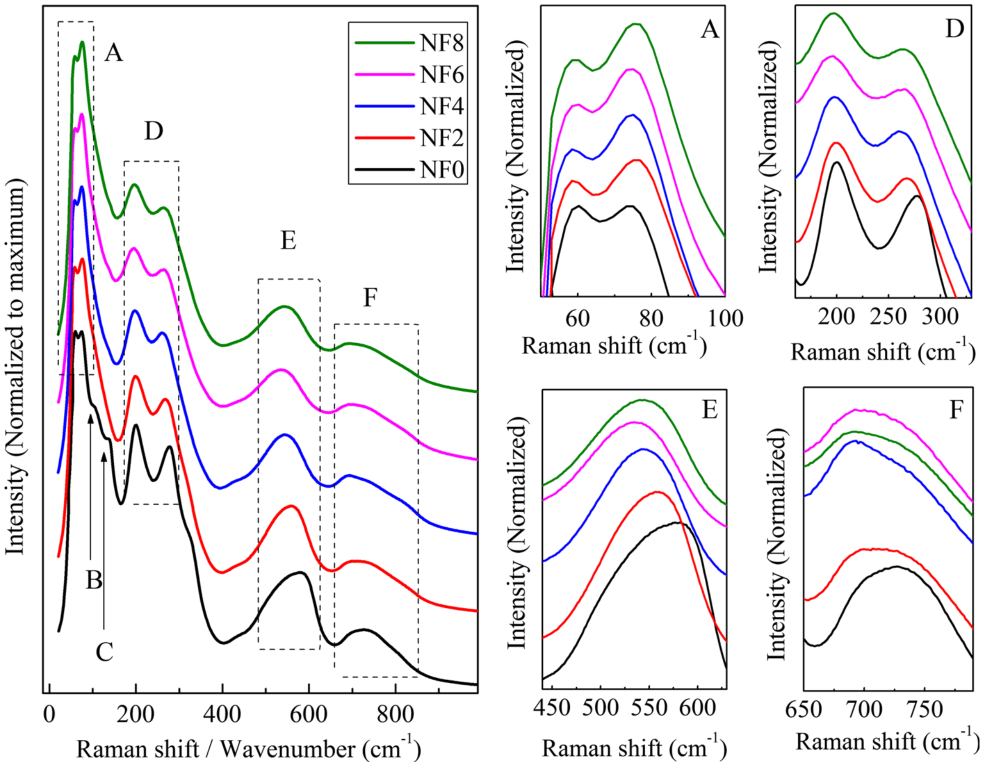

Figure 4 Raman spectra of Nb and Fe co-doped PLZT. The *four panels* on the right side are the closer views of regions marked as *A*, *D*, *E* and *F* in the *left panel*. *B* and *C* are found to show two humps, which disappear upon Nb and Fe doping.

Table 1 Comparison of Raman spectroscopic results of NF0 (i.e., PLZT (2/52/48)) with earlier published results of similar structures

Phonon modes		Calculated for $PbTiO_3$		Observed in $PbTiO_3$			PZT (52/48)	PLZT (*x*/52/48)	NF0 PLZT (2/52/48)
		Freire and Katiyar [30]	Hermet et al. [31]	Freire and Katiyar [30]	Foster et al. [32]	Fontana et al. [33]	Buixaderas et al. [34].	Yang et al. [28]	Present work
A_1	TO1	119	151	147	149	148	142	88	138
	LO1	167	189	189	194			156	
	TO2	301	357	359	359	362	307	324	330
	LO2	514	442	465	465		471	503	507
	TO3	578	653	646	647	650	569	594	596
	LO3	763	791	796	795		765	749	767
E	TO1	97	78	88	87	89	60		76
	LO1	149	117	128	128	130	100	132	107
	TO2	259	199	220	219	220	201	197	201
	LO2	300	269	289	289	290	427	261	277
	TO3	305	269	289	289	290	520	261	277
	LO3	475	416	439	441	440	704	415	439
	TO4	553	482	505	505	508		546	558
	LO4	758	655	723	687	720		704	728
B_1/A_2		263	283	289	289		265	261	277
E	TA	50		59					57
E	TO	163		168					
A_1	TA	64		72					

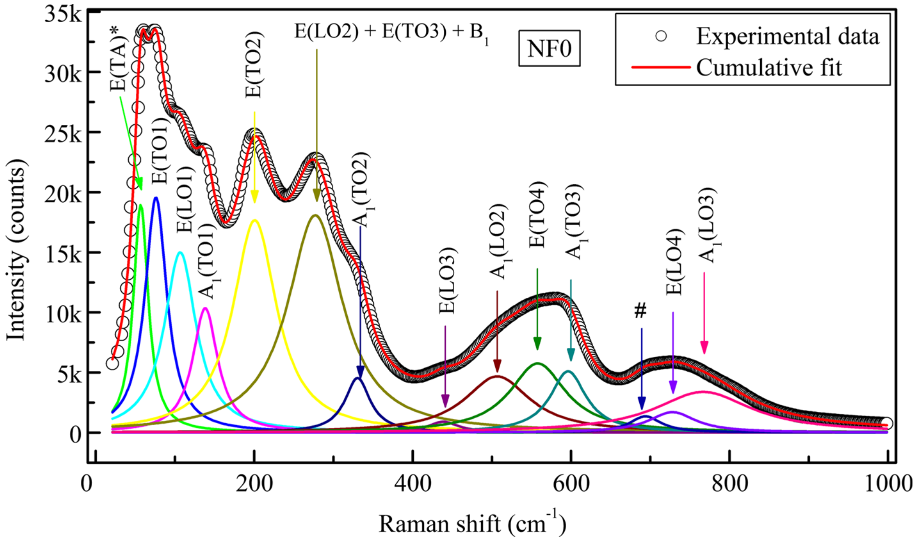

Figure 5 Cumulative fit (*red solid line*) of Raman spectroscopic data for NF0. The *colored lines* (except the *red line*) are the de-convoluted individual peaks. "#" and "*" marks represent unidentified and unconfirmed peaks.

The peak found in fit around 694 cm^{-1} is still unidentified and is shown with a "#" mark (Fig. 5).

Cumulative fit and de-convoluted peaks for Raman spectra of NF2, NF4, NF6 and NF8 are shown in Fig. 6. From these detailed analyses, it is found that *E*(TO2) and A_1(TO3) modes exhibit redshift upon Nb and Fe doping, which is similar to that observed in Fig. 4. Up to 6% doping, the phonon softening happens gradually (Fig. 7). For NF0, the *E*(TO2) mode frequency is near 201 cm^{-1}, which shifts to below 193 cm^{-1} for NF6. Similarly, the A_1(TO3) mode shifts from 596 to 555 cm^{-1}. It is interesting to note that both the modes shifted toward higher energy on further doping. For NF8 (i.e., 8 mol% Nb- and Fe-doped PLZT), the peak positions become 195.5 and 558.5 cm^{-1}, respectively. To understand the change, schematic two-dimensional diagrams are drawn for these two vibrations as shown in Fig. 7b. The *E*(TO2) mode corresponds to the vibration of central B (in ABO_3 perovskite) atom (Zr/Ti/Nb/Fe) against the

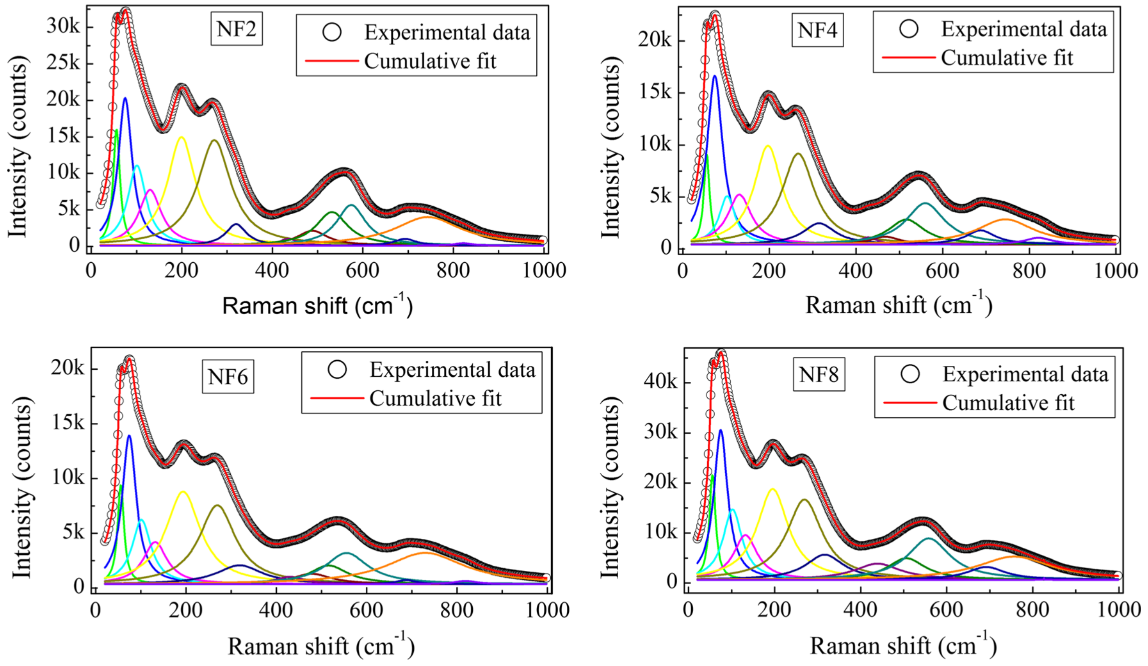

Figure 6 Cumulative fit (*red solid line*) of experimental Raman spectroscopic data for NF2, NF4 NF6 and NF8. The *colored lines* (except the *red line*) are the de-convoluted individual peaks.

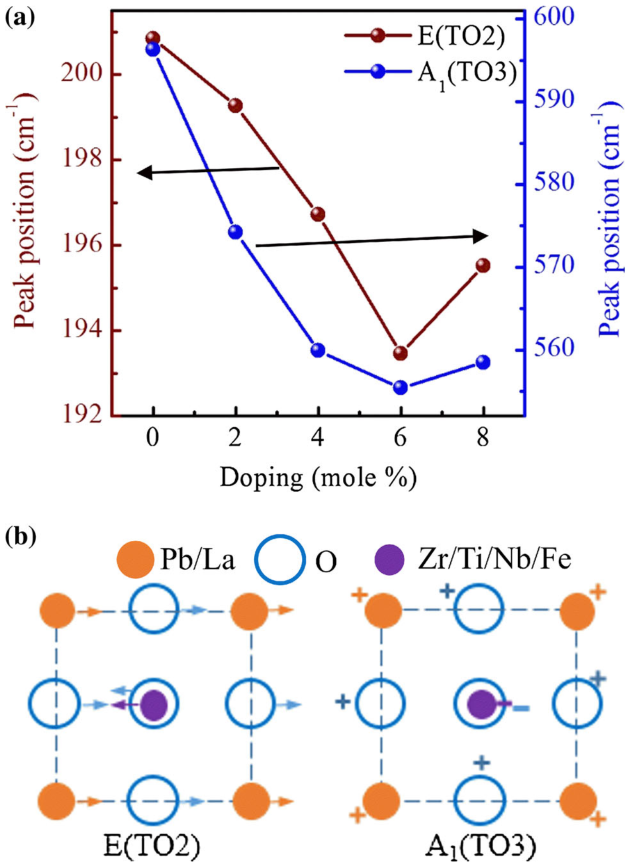

Figure 7 **a** Redshift of E(TO2) and A_1(TO3) modes. **b** Schematic diagram of E(TO2) and A_1(TO3) mode vibrations viewed along c-axis.

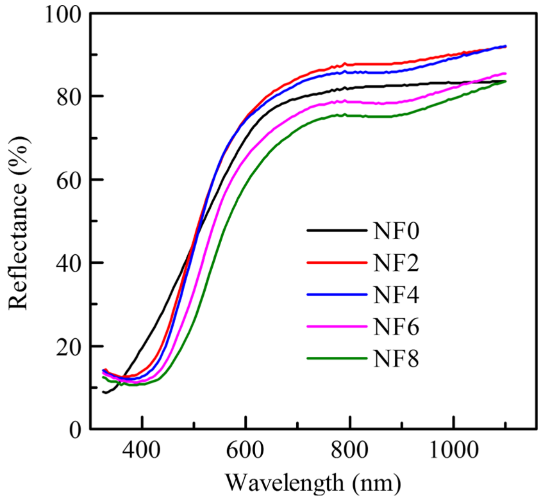

Figure 8 Diffuse reflectance spectra for NF0, NF2, NF4, NF6 and NF8.

octahedron in which all other atoms vibrate in opposite direction. The E(TO2) mode vibration is perpendicular to the polarization. In case of A_1(TO3) mode, the vibration occurs in a similar way but parallel to polarization, i.e., along c-axis.

Though the E(TO2) and A_1(TO3) vibrations are perpendicular to each other, they show similar characteristic changes which can be correlated with the fact of decreasing lattice parameters, a and c. This is a direct consequence of Nb and Fe co-doping.

Band gap study

In order to observe band gap and related changes due to co-doping of Nb and Fe, diffuse reflectance spectroscopy (DRS) is carried out. Figure 8 shows reflectance (R) at room temperature in the wavelength range from 325 to 1100 nm for NF0, NF2, NF4, NF6 and NF8. A distinct change in the optical properties of PLZT nanoparticles due to the addition of Nb and Fe is observed from these studies. Reflectance edge shifts toward higher wavelength, which is an outcome of the increasing ability of absorption of lower energy photons by the materials. This indicates that there is a decrement in the band gap (effective band gap) by substitution of Nb and Fe ions in PLZT lattice. For quantitative analysis, the Kubelka–Munk function $F(R) = \frac{(1-R)^2}{2R}$ has been calculated and plots of $(F(R)h\nu)$ versus $h\nu$ are shown in Fig. 9a. Here h is Planck's constant and ν, the frequency of radiation. These curves show sharp transition between 400 and 500 nm indicating the photon energy required/emitted for electronic transitions. The energy intercept of linear portion of the curve gives the value of band gap of the material. The band gap of NF0 calculated is 3.21 eV.

Undoped PZT shows band gap in the range around 2.6–3.5 eV [35], which may further depending on morphology, composition, processing, etc. [36]. Calculation shows that the band gap of PZT can vary from 3.45 to 3.72 eV [37]. For compositions PZT(52/48), i.e., around MPB, it is around 3.5 eV. Experimentally, it is observed that PZT prepared at 700 °C exhibits a band gap of 3.39 eV [38] while similar composition shows the values of band gap 3.36 and 3.38 eV, respectively, for band gaps in case of the samples prepared at 700 and 800 °C, respectively [39]. La doping could lower the band gap. As a result, it is seen that the band gap of NF0 (which is 2% La-doped PZT(52/48)) is 3.21 eV. The calculated values of band gap of NF2, NF4, NF6 and NF8 are 2.74, 2.70, 2.64 and 2.59 eV, respectively. The variation in band gap with doping concentration is plotted in Fig. 9b. The blueshift due to filling of near band gap states by heavy doping in a semiconductor is known as Burstein–Moss shift [40]. A schematic diagram (Fig. 9c) of band gap shrinkage due to the introduction of Nb and Fe in PLZT lattice has been drawn with the help of mechanism behind Burstein–Moss shift and is supported by photoluminescence (PL) experimental results (discussed below).

Photoluminescence (PL) emission spectra observed using an excitation wavelength of 325 nm (i.e., of energy 3.81 eV) are shown in Fig. 9d. Three broad peaks are found around 470 nm (2.64 eV), 482 nm (2.57 eV) and 492 nm (2.52 eV) which are almost consistent in energy for all the samples. This indicates that Nb and Fe doping does not affect the energy levels involved in these transitions. A broader peak observed at lower energy (2.3–2.45 eV) exhibits a redshift with increasing doping concentration. The position of the peak is 518 nm (2.39 eV), 522 nm (2.38 eV), 525 nm (2.36 eV), 528 nm (2.35 eV) and 532 nm (2.33 eV) for NF0, NF2, NF4, NF6 and NF8, respectively. The relative intensity of this particular peak with respect to the other three peaks (2.64, 2.57 and 2.52 eV) is found to increase as doping concentration increases.

Defects, such as Pb vacancies, O vacancies, Pb–O vacancy complex centers, the displacement of the Ti and distortion of TiO_6 octahedra, are considered to have importance in the mechanisms responsible for PL at room temperature in ABO_3-type materials [41, 42]. Pb evaporation during heat treatment of any Pb-based material is a well-known phenomenon. Pb evaporates as PbO creating Pb and O deficiency in the material. According to Eyraud's model [36, 39, 43, 44], when Pb evaporates as PbO, it leaves Pb and O vacancies which may create acceptors and donors in the following way:

$$V_{Pb} \rightarrow V'_{Pb} + e', V'_{Pb} \rightarrow V''_{Pb} + e', V_O \rightarrow V^{\cdot}_O + e' \text{ and } V^{\cdot}_O \rightarrow V^{\cdot\cdot}_O + e'$$

Energy of defects such as V'_{Pb}, V''_{Pb}, $V^{\cdot}_O$ and $V^{\cdot\cdot}_O$ (symbols for single and doubly ionized lead and oxygen vacancies) stay in the forbidden region, just below the minimum of conduction band and/or just above maximum of valence band [43]. Depending on the availability of the energy levels (mid-band gap

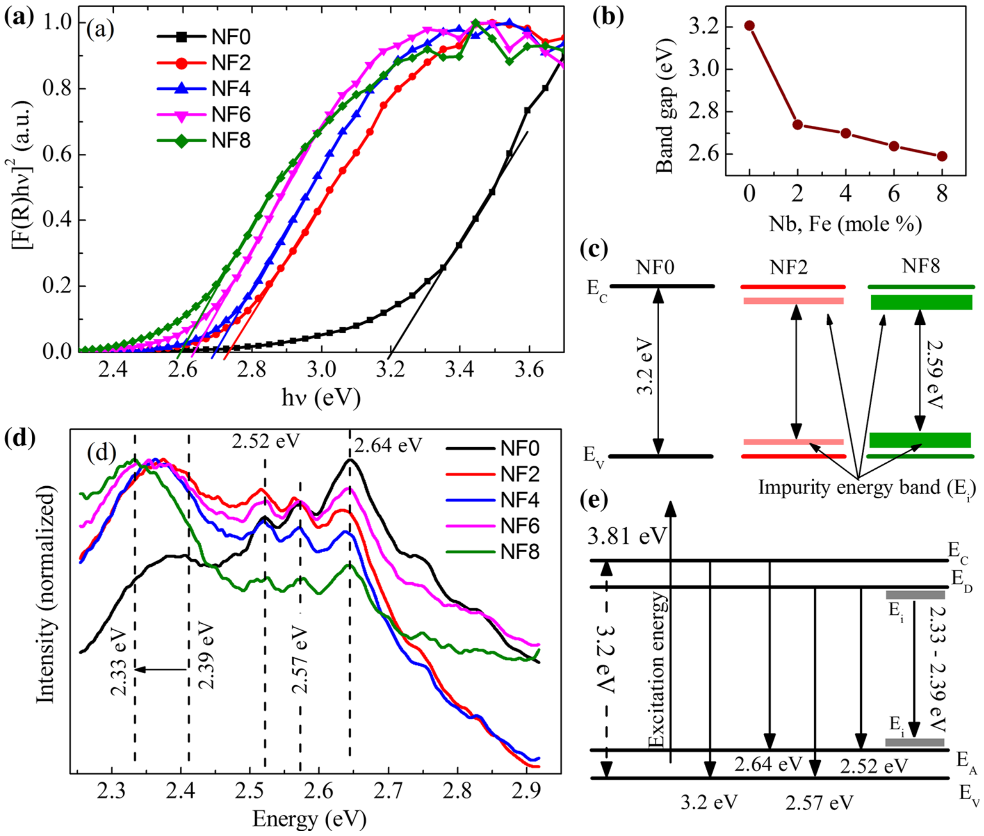

Figure 9 Band gap of NF0, NF2, NF4, NF6 and NF8. **a** Kubelka–Munk plot for determination of band gap. **b** Change in band gap due to increasing Nb and Fe doping concentration. **c** Schematic representation of band gap decrement by impurity energy band induced by Nb and Fe. **d** PL spectra of the samples. **e** Schematic of the mechanism of PL emissions as observed in (**c**).

states) created by these vacancies, there can be multiple absorption processes by these defect states leading to a number of PL emissions peaks, if the excitation energy is sufficient. The four most possible transitions (3.2, 2.64, 2.57 and 2.52 eV) for an excitation of 3.81 eV ($\sim$325 nm) are shown in the schematic diagram. The vacancy defects are due to evaporation of Pb, which strongly depends on the temperature of preparation and La doping. Higher temperature creates more Pb loss, and La^{3+} in place of Pb^{2+} also creates lead vacancies to compensate extra charge. However, as the preparation temperature and the amount of La are the same for all the five samples (NF0, NF2, NF4, NF6 and NF8), the energy bands created by Pb and O vacancies are expected to remain constant for all the samples. As a result, we do not see any change in PL spectra for the three peaks around 2.64, 2.57 and 2.52 eV. The transition at 3.2 eV has not been observed in the spectra as it is beyond the experimental range. The fourth peak in PL spectra (2.30–2.45 eV) is strongly affected by Nb and Fe. The peak intensity increases, and it shifts toward lower energy as doping concentration increases. These effects indicate that this emission is associated with the impurity level induced by Nb and Fe in addition to that induced by La already. As the doping concentration increases, the width of the impurity level increases. Hence, the effective band gap reduces. As a result, a change in band gap is observed (Fig. 9a, b); an effect is known as Burstein–Moss shift as explained above. As the width increases, the effective band gap reduces and the number of transitions associated with it increases. As a result, the relative intensity increases and redshift (2.39–2.33 eV in Fig. 9c) occurs.

Conclusions

Up to 8 mol% of Nb and Fe are simultaneously doped in PLZT. The XRD study confirms the successful incorporation of Nb and Fe in PLZT lattice. The lattice parameters are found to decrease gradually with increasing doping concentration. A total of 14 modes are observed from Raman spectral analysis, which have frequencies close to the theoretically calculated frequencies. Upon doping, a regular redshift is observed in several modes. Soft phonon modes show relative intensity change due to the presence of Nb and Fe. The effective band gap change due to 2% Nb and Fe co-doping shows a decrease from 3.21 to 2.74 eV. The band gap decreases further down to 2.59 eV upon doping of 8 mol%. The PL study satisfactorily explains the mechanism behind the changes observed.

Acknowledgements

This work has been supported by Japan Student Services Organization (JASSO), Shibaura Institute of Technology (SIT) under the Top Global University Project, Designed by Ministry of Education, Culture, Sports, Science and Technology in Japan and IIT Madras, India. The authors would like to acknowledge the support extended by Mr. Subhajit Nandy and Dr. Sudakar Chandran (Department of Physics, IIT Madras) in carrying out DRS measurements.

Compliance with ethical standards

Conflict of interest The authors declare that they have no conflict of interest.

References

[1] Ahart M, Somayazulu M, Cohen RE et al (2008) Origin of morphotropic phase boundaries in ferroelectrics. Nature 451:545–548

[2] Chen HD, Udayakumar KR, Gaskey CJ, Cross LE (1995) Electrical properties' maxima in thin films of the lead zirconate–lead titanate solid solution system. Appl Phys Lett 67:3411–3413

[3] Bouzid A, Bourim EM, Gabbay M, Fantozzi G (2005) PZT phase diagram determination by measurement of elastic moduli. J Eur Ceram Soc 25:3213–3221

[4] Baik S, Lee SM (1994) R-curve behaviour of PZT ceramics near the morphotropic phase boundary. J Mater Sci 29:6115–6122. doi:10.1007/BF00354550

[5] Bell AJ (2006) Factors influencing the piezoelectric behaviour of PZT and other "morphotropic phase boundary" ferroelectrics. J Mater Sci 41:13–25. doi:10.1007/s10853-005-5913-9

[6] Scott JF (2007) Data storage. Multiferroic memories. Nat Mater 6:256–257

[7] Xu B, Yin KB, Lin J et al (2009) Room-temperature ferromagnetism and ferroelectricity in Fe-doped $BaTiO_3$. Phys Rev B 79:134109-1–134109-5

[8] Kleebe H-J, Lauterbach S, Silvestroni L, Kungl H, Hoffmann MJ, Erdem E, Eichel Rd-A (2009) Formation of

magnetic grains in ferroelectric Pb[$Zr_{0.6}Ti_{0.4}$]O_3 ceramics doped with Fe^{3+} above the solubility limit. Appl Phys Lett 94:142901-1–142901-3

[9] Zhou J-p, He H-c, Shi Z, Liu G, Nan C-W (2006) Dielectric, magnetic, and magnetoelectric properties of laminated $PbZr_{0.52}Ti_{0.48}O_3/CoFe_2O_4$ composite ceramics. J Appl Phys 100:094106-1–094106-6

[10] Amonpattaratkit P, Jantaratana P, Ananta S (2015) Influences of PZT addition on phase formation and magnetic properties of perovskite Pb($Fe_{0.5}Nb_{0.5}$)O_3-based ceramics. J Magn Magn Mater 389:95–100

[11] Lisnevskaya IV, Bobrova IA, Lupeiko TG, Agamirzoeva MR, Myagkaya KV (2016) Y3Fe5O12/Na, Bi, Sr-doped PZT particulate magnetoelectric composites. J Magn Magn Mater 405:62–65

[12] Zhai J, Cai N, Shi Z, Lin Y, Nan C-W (2004) Magnetic-dielectric properties of $NiFe_2O_4$/PZT particulate composites. J Phys D Appl Phys 37:823–827

[13] Song Y, Da Pan LXu, Liu B, Volinsky AA, Zhang S (2016) Enhanced magnetoelectric efficiency of the $Tb_{1-x}Dy_xFe_{2-y}$/Pb(Zr, Ti)O_3 cylinder multi-electrode composites. Mater Des 90:753–756

[14] Wang J, Wu X, Deng C, Zhu K, Qiu J (2016) The effect of $LaNiO_3$ thickness on the magnetoelectric response of Pb($Zr_{0.52}Ti_{0.48}$)O_3 film-on-$CoFe_2O_4$ ceramic composites. J Mater Sci 52:541–549. doi:10.1007/s10853-016-0352-3

[15] Schiemer JA, Lascu I, Harrison RJ et al (2016) Elastic and anelastic relaxation behaviour of perovskite multiferroics I: $PbZr_{0.53}Ti_{0.47}O_3$ (PZT)–$PbFe_{0.5}Nb_{0.5}O_3$ (PFN). J Mater Sci 51:10727–10760. doi:10.1007/s10853-016-0280-2

[16] Schiemer JA, Lascu I, Harrison RJ et al (2017) Elastic and anelastic relaxation behaviour of perovskite multiferroics II: $PbZr_{0.53}Ti_{0.47}O_3$ (PZT)–$PbFe_{0.5}Ta_{0.5}O_3$ (PFT). J Mater Sci 52:285–304. doi:10.1007/s10853-016-0330-9

[17] Schiemer J, Carpenter MA, Evans DM et al (2014) Studies of the room-temperature multiferroic Pb($Fe_{0.5}Ta_{0.5}$)$_{0.4}$($Zr_{0.53}Ti_{0.47}$)$_{0.6}O_3$: resonant ultrasound spectroscopy, dielectric, and magnetic phenomena. Adv Funct Mater 24:2993–3002

[18] Lima KCV, Filho AGS, Ayala AP, Filho J, Mendes Freire PTC, Melo FEA, Araújo EB, Eiras JA (2001) Raman study of morphotropic phase boundary in $PbZr_{1-x}Ti_xO_3$ at low temperatures. Phys Rev B 63:184105-1–184105-5

[19] Rouquette J, Haines J, Bornand V, Pintard M, Papet Ph, Astier R, Léger JM, Gorelli F (2002) Transition to a cubic phase with symmetry-breaking disorder in $PbZr_{0.52}Ti_{0.48}O_3$ at high pressure. Phys Rev B 65:214102-1–214102-4

[20] Haines J, Rouquette J, Bornand V, Pintard M, Papet P, Gorelli FA (2003) Raman scattering studies at high pressure and low temperature: technique and application to the piezoelectric material $PbZr_{0.52}Ti_{0.48}O_3$. J Raman Spectrosc 34:519–523

[21] Sani A, Noheda B, Kornev IA, Bellaiche L, Bouvier P, Kreisel J (2004) High-pressure phases in highly piezoelectric $PbZr_{0.52}Ti_{0.48}O_3$. Phys Rev B 69:020105-1–020105-4. doi:10.1103/PhysRevB.69.020105

[22] Osada M, Nishida K, Wada S, Okamoto S, Ueno R, Funakubo H, Katoda T (2005) Domain distributions in tetragonal Pb(Zr, Ti)O_3 thin films probed by polarized Raman spectroscopy. Appl Phys Lett 87:232902-1–232902-3

[23] Efimov VV, Efimova EA, Iakoubovskii K et al (2006) EXAFS, X-ray diffraction and Raman studies of ($Pb_{1-x}La_x$)($Zr_{0.65}Ti_{0.35}$)O_3 ($x = 0.04$ and 0.09) ceramics irradiated by high-current pulsed electron beam. J Phys Chem Solids 67:2007–2012

[24] Rouquette J, Haines J, Bornand V, Pintard M, Papet P, Sauvajol JL (2006) Use of resonance Raman spectroscopy to study the phase diagram of $PbZr_{0.52}Ti_{0.48}O_3$. Phys Rev B 73:224118-1–224118-5

[25] Zhang Y, Cheng X, Zhang S (2007) In-situ Raman spectroscopic study of domain switching of PLZT ceramics. Appl Phys A 89:685–693

[26] Shannigrahi SR, Tripathy S (2007) Micro-Raman spectroscopic investigation of rare earth-modified lead zirconate titanate ceramics. Ceram Int 33:595–600

[27] Buixaderas E, Gregora I, Kamba S, Petzelt J, Kosec M (2008) Raman spectroscopy and effective dielectric function in PLZT x/40/60. J Phys: Condens Matter 20:345229-1–345229-10

[28] Yang F-J, Cheng X, Zhou Z-D, Zhang Y (2009) An analysis of domain reorientation in PLZT ceramics by in situ Raman spectroscopy. J Appl Phys 106:114115-1–114115-5

[29] Li J-F, Zhu Z-X, Lai F-P (2010) Thickness-dependent phase transition and piezoelectric response in textured Nb-doped Pb($Zr_{0.52}Ti_{0.48}$)O_3 thin films. J Phys Chem C 114:17796–17801

[30] Freire JD, Katiyar RS (1988) Lattice dynamics of crystals with tetragonal $BaTiO_3$ structure. Phys Rev B 37:2074–2085

[31] Hermet P, Veithen M, Ghosez P (2009) Raman scattering intensities in $BaTiO_3$ and $PbTiO_3$ prototypical ferroelectrics from density functional theory. J Phys: Condens Matter 21:215901-1–215901-10

[32] Foster CM, Li Z, Grimsditch M, Chan SK, Lam DJ (1993) Anharmonicity of the lowest-frequency A_1(TO) phonon in $PbTiO_3$. Phys Rev B 48:10160–10167

[33] Fontana M, Idrissi H, Kugel G, Wojcik K (1991) Raman spectrum in $PbTiO_3$ re-examined: dynamics of the soft phonon and the central peak. J Phys: Condens Matter 3:8695–8706

[34] Buixaderas E, Bovtun V, Kempa M, Nuzhnyy D, Savinov M, Vanek P, Gregora I, Malic B (2016) Lattice dynamics and domain wall oscillations of morphotropic Pb(Zr, Ti)O_3 ceramics. Phys Rev B 94:054315-1–054315-10

[35] Nagaraj B, Aggarwal S, Song TK, Sawhney T, Ramesh R (1999) Leakage current mechanisms in lead-based thin-film ferroelectric capacitors. Phys Rev B 59:16022–16027

[36] Durruthy-Rodríguez MD, Costa-Marrero J, Hernández-García M, Calderón-Piñar F, Yañez-Limón JM (2009) Photoluminescence in “hard” and “soft” ferroelectric ceramics. Appl Phys A 98:543–550

[37] Robertson J, Warren WL, Tuttle BA (1995) Band states and shallow hole traps in Pb(Zr, Ti)O_3 ferroelectrics. J Appl Phys 77:3975–3980

[38] Ghasemifard M, Hosseini SM, Khorsand Zak A, Khorrami GH (2009) Microstructural and optical characterization of PZT nanopowder prepared at low temperature. Phys E 41:418–422

[39] Rodríguez-Aranda MC, Calderón-Piñar F, Hernández-Landaverde MA, Heiras J, Zamorano-Ulloa R, Ramírez-Rosales D, Yáñez-Limón JM (2016) Photoluminescence of sol–gel synthesized PZT powders. J Lumin 179:280–286

[40] Peter Y, Cardona M (2010) Fundamentals of semiconductors: physics and materials properties. Springer, Berlin. doi:10.1007/978-3-642-00710-1

[41] Silva MS, Cilense M, Orhan E et al (2005) The nature of the photoluminescence in amorphized PZT. J Lumin 111:205–213

[42] Anicete-Santos M, Silva MS, Orhan E, Góes MS, Zaghete MA, Paiva-Santos CO, Pizani PS, Cilense M, Varela JA, Longo E (2007) Contribution of structural order–disorder to the room-temperature photoluminescence of lead zirconate titanate powders. J Lumin 127:689–695

[43] Eyraud L, Guiffard B, Lebrun L, Guyomar D (2006) Interpretation of the softening effect in PZT ceramics near the morphotropic phase boundary. Ferroelectrics 330:51–60

[44] Hernández-García M, Durruthy-Rodríguez MD, Costa-Marrero J, Calderón-Piñar F, Guerra JDS, Yañez-Limón JM (2014) Photoluminescence in $Pb_{0.95}Sr_{0.05}(Zr_{1-x}Ti_x)_{1-y}Cr_y$-$O_3$ ferroelectric ceramic system. J Appl Phys 116:043510-1–043510-6